AFRL-RX-WP-JA-2014-0177

REACTIVE SPARK PLASMA SINTERING (SPS) OF NITRIDE REINFORCED TITANIUM ALLOY COMPOSITES (POSTPRINT)

Jaimie S. Tiley
AFRL/RXCM

SEPTEMBER 2014
Interim Report

STINFO COPY

AIR FORCE RESEARCH LABORATORY
MATERIALS AND MANUFACTURING DIRECTORATE
WRIGHT-PATTERSON AIR FORCE BASE, OH 45433-7750
AIR FORCE MATERIEL COMMAND
UNITED STATES AIR FORCE

NOTICE AND SIGNATURE PAGE

_____//Signature//_____   _____//Signature//_____
JAIMIE S. TILEY   DANIEL J. EVANS, Chief
Metals Branch   Metals Branch
Structural Materials Division   Structural Materials Division

_____//Signature//_____
TIMOTHY J. SCHUMACHER, Chief
Structural Materials Division
Materials and Manufacturing Directorate

REPORT DOCUMENTATION PAGE

1. REPORT DATE (DD-MM-YYYY) September 2014	2. REPORT TYPE Interim	3. DATES COVERED *(From – To)* 19 March 2014 – 05 August 2014

4. TITLE AND SUBTITLE
REACTIVE SPARK PLASMA SINTERING (SPS) OF NITRIDE REINFORCED TITANIUM ALLOY COMPOSITES (POSTPRINT)

5a. CONTRACT NUMBER
In-House

5b. GRANT NUMBER

5c. PROGRAM ELEMENT NUMBER
62102F

6. AUTHOR(S)
(see back)

5d. PROJECT NUMBER
4349

5e. TASK NUMBER

5f. WORK UNIT NUMBER
X0W6

7. PERFORMING ORGANIZATION NAME(S) AND ADDRESS(ES)
(see back)

8. PERFORMING ORGANIZATION REPORT NUMBER

9. SPONSORING / MONITORING AGENCY NAME(S) AND ADDRESS(ES)
Air Force Research Laboratory
Materials and Manufacturing Directorate
Wright Patterson Air Force Base, OH 45433-7750
Air Force Materiel Command
United States Air Force

10. SPONSOR/MONITOR'S ACRONYM(S)
AFRL/RXCM

11. SPONSOR/MONITOR'S REPORT NUMBER(S)
AFRL-RX-WP-JA-2014-0177

12. DISTRIBUTION / AVAILABILITY STATEMENT
Distribution A. Approved for public release; distribution unlimited. This report contains color.

14. ABSTRACT
Coupled in situ alloying and nitridation of titanium–vanadium alloys, has been achieved by introducing reactive nitrogen gas during the spark plasma sintering (SPS) of blended titanium and vanadium elemental powders, leading to a new class of nitride reinforced titanium alloy composites. The resulting microstructure includes precipitates of the δ-TiN phase with the NaCl structure, equiaxed (or globular) precipitates of a nitrogen enriched hcp α(Ti,N) phase with a c/a ratio more than what is expected for pure hcp Ti, and fine scale plate-shaped precipitates of hcp α-Ti, distributed within a bcc β matrix. During SPS processing, the δ-TiN phase appears to form at a temperature of 1400℃, while only hcp α(Ti,N) and α-Ti phases form at lower processing temperatures. Consequently, the highest microhardness is exhibited by the composite processed at 1400℃ while those processed at 1300℃ or below exhibit lower values. Processing at temperatures below 1300℃, resulted in an incomplete alloying of the blend of titanium and vanadium powders. These δ-TiN precipitates act as heterogeneous nucleation sites for the α(Ti,N) precipitates that appear to engulf and exhibit an orientation relationship with the nitride phase at the center. Furthermore, fine scale α-Ti plates are precipitated within the nitride precipitates, presumably resulting from the retrograde solubility of nitrogen in titanium.

15. SUBJECT TERMS
metal–matrix composites (MMCs), sintering, microstructure, transmission electron microscopy (TEM), synchrotron radiation

16. SECURITY CLASSIFICATION OF:			17. LIMITATION OF ABSTRACT	18. NUMBER OF PAGES	19a. NAME OF RESPONSIBLE PERSON *(Monitor)* Jaimie S. Tiley
a. REPORT Unclassified	**b. ABSTRACT** Unclassified	**c. THIS PAGE** Unclassified	SAR	17	**19b. TELEPHONE NUBER** *(include area code)* (937) 255-7416

REPORT DOCUMENTATION PAGE Cont'd

6. AUTHOR(S)

Jaimie S. Tiley - Materials and Manufacturing Directorate, Air Force Research Laboratory, Structural Materials Division

Tushar Borkar and Rajarshi Banerjee - Center for Advanced Research and Technology and Department of Materials Science and Engineering, University of North Texas

Yang Ren - X-ray Science Division, Advanced Photon Source, Argonne National Laboratory

Soumya Nag - CMT Structural and Functional Metals Lab, GE Global Research Center

7. PERFORMING ORGANIZATION NAME(S) AND ADDRESS(ES)

AFRL/RXCM
Air Force Research Laboratory
Materials and Manufacturing Directorate
Wright-Patterson Air Force Base, OH 45433-7750

Center for Advanced Research and Technology
Department of Materials Science and Engineering
University of North Texas
Denton, TX 76203

X-ray Science Division
Advanced Photon Source
Argonne National Laboratory, IL 60439

CMT Structural and Functional Metals Lab
GE Global Research Center
Niskayuna, NY 12309

Reactive spark plasma sintering (SPS) of nitride reinforced titanium alloy composites

Tushar Borkar [a], Soumya Nag [a,d], Yang Ren [b], Jaimie Tiley [c], Rajarshi Banerjee [a,*]

[a] Center for Advanced Research and Technology and Department of Materials Science and Engineering, University of North Texas, Denton 76203, USA
[b] X-ray Science Division, Advanced Photon Source, Argonne National Laboratory, IL 60439, USA
[c] Materials and Manufacturing Directorate, Air Force Research laboratory, Dayton, OH 45433, USA
[d] CMT Structural and Functional Metals Lab, GE Global Research Center-Niskayuna, NY 12309, USA

A B S T R A C T

Coupled in situ alloying and nitridation of titanium–vanadium alloys, has been achieved by introducing reactive nitrogen gas during the spark plasma sintering (SPS) of blended titanium and vanadium elemental powders, leading to a new class of nitride reinforced titanium alloy composites. The resulting microstructure includes precipitates of the δ-TiN phase with the NaCl structure, equiaxed (or globular) precipitates of a nitrogen enriched hcp α(Ti,N) phase with a c/a ratio more than what is expected for pure hcp Ti, and fine scale plate-shaped precipitates of hcp α-Ti, distributed within a bcc β matrix. During SPS processing, the δ-TiN phase appears to form at a temperature of 1400 °C, while only hcp α(Ti,N) and α-Ti phases form at lower processing temperatures. Consequently, the highest microhardness is exhibited by the composite processed at 1400 °C while those processed at 1300 °C or below exhibit lower values. Processing at temperatures below 1300 °C, resulted in an incomplete alloying of the blend of titanium and vanadium powders. These δ-TiN precipitates act as heterogeneous nucleation sites for the α(Ti,N) precipitates that appear to engulf and exhibit an orientation relationship with the nitride phase at the center. Furthermore, fine scale α-Ti plates are precipitated within the nitride precipitates, presumably resulting from the retrograde solubility of nitrogen in titanium.

© 2014 Elsevier B.V. All rights reserved.

1. Introduction

Titanium and titanium alloys possess several excellent as well as attractive properties, such as high strength to weight ratio (specific strength) [1–6], low specific weight (low density) [5–8], good corrosion resistance [1–6,8–12], excellent ductility & formability (good balance of mechanical properties) [5,12–14], low rate of metal ion release and very reduced cell or tissue reaction [8], and heat resistance (high thermal capacity) [3,5]. Thus these alloys are suitable candidates for structural [15] aerospace [2–5], marine [16], automotive, biomedical (such as in dental and orthopedic as bone implants) [1–6,8–12,15–20], and other industrial applications [21–25]. Titanium is widely used in the medical field to replace heart valves, joints, and bones for dental prosthetics due to its excellent strength and biocompatibility [16]. However, titanium and titanium alloys typically exhibit less than optimal tribological properties such as poor abrasive wear resistance, poor fretting behavior, high coefficient of friction, and poor surface hardness,

which limit its use in mechanical engineering applications as well as in articulating components of hip and knee prostheses [3–5,7,8,10,11,13,16–18]. The tribological properties of titanium alloys can be potentially improved by reinforcing it with hard precipitates, such as titanium nitride (TiN), that exhibits unique properties such as extreme hardness, high chemical and physical stability, good thermal and electrical conductivity, high melting point, good resistance to wear and corrosion, excellent biocompatibility, and excellent performance as an adhesion layer. All of these factors make TiN a promising reinforcement for metal–matrix composites for a variety of applications, including tribological coatings, cutting tools, automotive, nuclear energy, and even microelectronic applications [1,4,5,7,8,10–14,16,25–34]. Therefore, nitriding of titanium alloys can improve the surface hardness and fatigue crack initiation resistance, and it has a great potential to expand the field of applications, such as coating for the heads of hip prostheses to improve their wear and fatigue resistance, hard coatings for dental implants and dental surgery tools, tribological orthopedic devices, gears, valves, pumps, and numerous other engineering components involving two surfaces in contact under load and in relative motion [7,16,25,26,29,34]. TiN surface layer

* Corresponding author. Tel.: +1 940 891 6812; fax: +1 940 565 4824.
  E-mail address: Rajarshi.Banerjee@unt.edu (R. Banerjee).

can be fabricated on titanium alloys by various methods, including physical vapor deposition (PVD), chemical vapor deposition (CVD), ion implantation, plasma nitriding, reactive sputtering, pulse ion implantation, powder immersion reaction assisted coating nitriding, and laser gas nitriding (LGN) [4,10–13,35]. Most of these techniques have their drawbacks, in terms of formation of brittle coatings on the surface, the thickness of which is severely restricted by low diffusivity of nitrogen [10–13,35]. Also in a previous study, nitridation of β Ti–Mo alloys was achieved in a gaseous N_2 atmosphere, forming continuous surface δ-TiN layer and a subsurface microstructure consisting of nitrogen-rich α(Ti,N) laths, dispersed within the β matrix [17,36]. While such surface nitridation via heating in the nitrogen atmosphere is a simple and cost-effective way to have a case-hardened layer, the time required and the depth of penetration are rather limited and it is difficult to introduce hard nitrides (or other nitrogen-enriched hard phases) within the bulk of the material [17,36]. Also, even though laser gas nitriding is a good way to achieve interfacial bonding with the substrate, TiN monolithic coatings have found little industrial application due to their inherent brittleness and inferior fracture toughness [6,10–13]. In contrast, metal matrix composites (MMCs) reinforced with hard precipitates exhibit superior properties compared to their monolithic counterparts in terms of fracture toughness, wear resistance, and mechanical strength [11]. Therefore, TiN reinforced titanium matrix composites can potentially obviate the above problems associated with monolithic TiN coatings [11]. The TiN reinforced titanium alloy composites may be fabricated using conventional powder metallurgical routes. Even though these samples show some improvement in mechanical and tribological properties, the composites prepared via the powder metallurgy route exhibit considerable amounts of residual porosity. Another probable technique is by direct introduction of nitride particles during laser deposition of titanium alloys. However, the quality of interface between such externally introduced reinforcements and alloy matrix can be rather difficult to control. This can also lead to issues like clustering of reinforced particles within the matrix, primarily due to difference in specific density between the matrix and particles, interfacial reactions, and poor wettability between reinforcements and matrix. In-situ nitridation process helps to overcome these issues encountered in an ex-situ nitridation process. The in-situ titanium matrix composites have the following advantage over conventional ex situ titanium matrix composites: (a) the TiN that is formed is thermodynamically stable, leading to less degradation under elevated temperatures, (b) the TiN particles are finer in size and are uniformly distributed within the matrix resulting in better mechanical properties, and (c) the precipitate/matrix interface is clean, resulting in strong interfacial bonding [3,15].

Spark plasma sintering (SPS) is a novel tool for in-situ processing of metal matrix composites at lower temperatures and shorter processing times as compared to conventional casting or infiltration processes [37–39]. In the SPS process, local high temperature state is generated when sparks discharge in a gap or at the contact point between the particles of powder causing evaporation and melting on the surface of powder particles, thus helping in the formation of fully dense composites. This initiation of the spark discharge in the gap between particles is assisted by fine impurities and gases on and between the surfaces of the particles [37–46]. SPS is a high-speed powder consolidation (sintering) technology capable of processing conductive and non-conductive materials, and it utilizes uniaxial force and on–off DC pulse energizing. This high frequency transfers and disperses the joule heat phenomenon throughout the specimen; resulting in a rapid and thorough heat distribution, ensuring high homogeneity and consistent precipitate densities [37–46]. Consolidation of nanopowders is possible in SPS without excessive grain growth due to the high heating rates and lower sintering times and temperatures involved [37–39]. While SPS is effective for any processing powders over wide size ranges, there is substantial current interest in using this technique for processing nanocrystalline materials. SPS also offers the ability to produce near-net shape components, which exhibit a symmetrical and simple geometry, in one step. However for complex shapes further machining may be required.

Based on the published literature on SPS processed materials, including composites, it appears that while this process has been employed as an effective technique for lower temperature sintering of powders to full density, there have been rather limited studies on in situ alloying and reactions during the SPS process. A recent study on SPS processing of hafnium carbide (HfC) starting from a blend of hafnium oxide (HfO_2) and carbon (C) powders, demonstrates the potential of this technique for in situ reactions resulting in compound formation [50]. The motivation of the present study is:

1. To investigate in situ alloying of elemental Ti and V powders, during SPS sintering.
2. To explore the possibility of in situ nitridation of Ti–V alloys by introducing reactive nitrogen gas during SPS processing.
3. To develop a detailed understanding of the microstructural evolution process in this Ti–V–N system during SPS processing.

2. Experimental details

In this study solid state sintering of Ti and V powders was conducted via spark plasma sintering (SPS) process. SPS sintering was carried out mainly in four stages, (i) removing existing unwanted gases and creating a vacuum, (ii) immediate introducing the protective argon or reactive nitrogen gas (for is situ nitridation) into the SPS chamber at high pressures, (iii) application of resistance heating and (iv) relieving of pressure and cooling the chamber. The detailed mechanism of this process has been reported elsewhere [37]. Commercially available pure titanium and vanadium powders in the ratio of Ti:V = 95:5 by weight were mixed using a twin-roller ball mill (using ball to powder ratio of 10:1) and then precompacted in a graphite die (dia. 20 mm) under a pressure of 5 MPa. Subsequently the precompacted specimens were sintered by SPS system model 10–3 manufactured by Thermal technology LLC under pure argon atmosphere (for the preparation of pure Ti–V) as well as under pure nitrogen atmosphere (to study the in situ nitridation of Ti–V alloy) at a uniaxial pressure of 65 MPa. The SPS processing parameters i.e. holding temperature and time are listed in Table 1. The heating rate for all cases was maintained at 200 °C/min and temperature was precisely monitored using pyrometer. As listed in the table, primarily two different temperatures were used for the current study. The Ti–V alloys that were sintered in pure argon atmosphere at 1100 °C, 1200 °C, 1300 °C and 1400 °C are denoted as Ti–V_x where x stands for the sintering temperature. Similarly the samples that went through the nitridation process due to compaction in nitrogen atmosphere at 1300 °C and 1400 °C are labeled as Ti–V–N_{1300} and Ti–V–N_{1400} respectively.

The microstructure of SPS processed samples was characterized in FEI Nova NanoSEM 230™ system. The instrument was also equipped with an electron backscatter detector (EBSD), where investigations of orientation relationships between the different phases observed in these composites were conducted. Analyses of these runs were done using the TSL OIM™ software. High-energy X-ray diffraction analysis of the composites was performed on the 11-IDC beamline (111 keV, λ = 0.111650 Å) of the Advanced Photon Source (APS) at Argonne National laboratory (ANL). A CeO_2 standard (NIST diffraction intensity standard set: 674a) was used to calibrate the sample-to-detector distance. The radiation scattered by the calibrant and samples was collected on a Perkin Elmer 2D detector system. The 2D diffraction data were integrated and converted to intensity versus 2θ using the program Fit-2D and further refined using GSAS and EXP-GUI program. The hardness of these specimens was measured using a standard Vickers microhardness tester where a load of 2.94 N was applied for 15 s. In each case an average of 10 readings were used for comparison. In addition to the SEM and high-energy XRD studies, the crystal structure of TiN precipitates was confirmed based on transmission electron microscopy (TEM) investigations. Site-specific TEM sample was prepared using a FEI Nova NanoLab 200™ focused ion beam instrument and was characterized in a FEI Tecnai F20™ FEG TEM operating at 200 keV.

3. Results and discussion

3.1. Optimization of SPS processing condition

A series of backscattered SEM images recorded from the Ti–V alloys for different processing temperatures and corresponding

2

Table 1
Calculated vanadium diffusion times for different temperatures for diffusion distances of 50, 100, and 200 μm and experimental SPS holding times for different temperatures.

Diffusion Distance (μm)	1100 °C (diff. time in min.)	1200 °C (diff. time in min.)	1300 °C (diff. time in min.)	1400 °C (diff. time in min.)
50	29.69	10.912	4.249	1.73
100	118.78	43.648	17.04	10.912
200	475.158	174.59	67.98	27.74
Experimental SPS holding time (min.)	15	45	60	30

$D = A_1 \exp(-Q_1/kT) + A_2 \exp(-Q_2/kT)$
Tracer impurity diffusion coefficients : (V in β Titanium)

$$\left.\begin{array}{l} A_1 = 3.4 \text{ cm}^2 \text{ s}^{-1} \\ A_2 = 1.0 \times 10^{-3} \text{ cm}^2 \text{ s}^{-1} \\ Q_1 = 257.5 \text{ kJ mol}^{-1} \\ Q_2 = 145.3 \text{ kJ mol}^{-1} \end{array}\right\} \text{"" "Smithells Metals Refence Book"[49]}$$
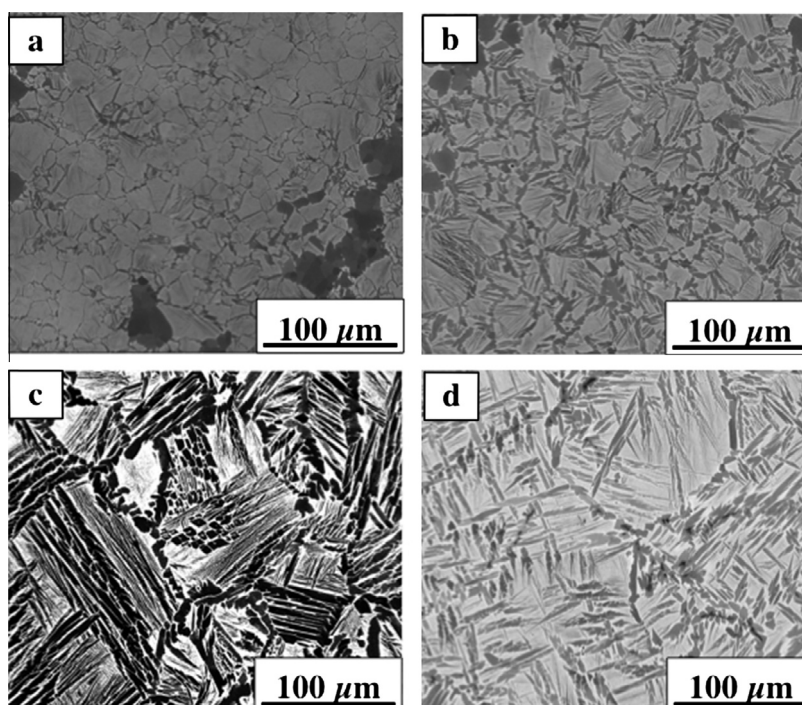
Fig. 1. Backscattered SEM image of SPS sintered Ti–V alloy in Ar atmosphere at (a) 1100° for 15 min (b) 1200° for 45 min (c) 1300° for 60 min and (d) 1400° for 30 min.

times (listed in Table 1) are shown in Fig. 1. Fig. 1(a) and (b) shows the microstructures of binary Ti–V alloy sintered under pure Ar atmosphere at 1100 °C for 15 min and at 1200 °C for 45 min respectively. Both these micrographs show uniformly distributed fine scale precipitates of a second phase; presumably α precipitates within the β-matrix with some un-reacted titanium powder particles. Both grain boundaries as well as intra-granular α precipitates are observed in both cases. It should be noted that these initial experiments were performed to optimize the parameters of SPS processing in order to obtain a fully dense as well as fully reacted Ti–V alloy exhibiting a uniform distribution of fine scale α precipitates within the β matrix. As SPS is a solid-state sintering process, the diffusivity of V in the β matrix of Ti, was considered to be an important factor in determining complete alloying and the formation of a desirable microstructure. Thus the diffusion distance and time required for V diffusion into β–Ti matrix at different temperatures and the corresponding SPS processing parameters were calculated and have been listed in Table 1. It is clear from this table that V atoms diffuse less than 100 μm for both heat treatment conditions (1100 °C for 15 min and 1200 °C for 45 min). As observed from the unreacted Ti powders in Fig. 1(a) and (b), it is clear that this time–temperature schedule is not sufficient to obtain a fully

reacted and homogeneous Ti–V alloy. Thus the diffusion times were calculated for different temperatures for a V diffusion distance of 200 μm, which is again listed in Table 1. Fig. 1(c) and (d) shows the microstructures for the binary Ti–V alloy sintered in a pure Ar atmosphere at 1300 °C for 60 min and at 1400 °C for 30 min respectively. The microstructure primarily consists of grain boundary α precipitates along with significant amount of intra-granular α laths within the β matrix. Interestingly, it appears that a bimodal distribution of α precipitates develops within the β grains. While complete alloying was observed in case of sintering at 1300 and 1400 °C, it was absent at lower sintering temperatures i.e. 1100 and 1200 °C exhibiting unreacted Ti particles. However, all four of these sintering temperatures are in the high temperature single β phase field of the Ti–V phase diagram. Hence the formation of intra-granular α precipitates is a consequence of the continuous cooling experienced during SPS processing after the completed homogenization and alloying within the single β phase has taken place at the sintering temperature. Due to the relatively fast cooling rate (∼40 °C/min) experienced during this process there is formation of both grain boundary α as well as intra-granular α precipitates. Based on these results, it is evident that 1300 °C for 60 min and 1400 °C for 30 min are optimized conditions for

3

achieving complete alloying in SPS for the Ti–5 wt%V system. Therefore, the subsequent studies on in situ nitridation, by introducing nitrogen gas into the SPS chamber, were carried out using these sintering conditions.

### 3.2. In situ nitridation during SPS processing

X-ray diffraction (XRD) patterns corresponding to the Ti–V alloys sintered at 1300 °C and 1400 °C under pure argon and under pure nitrogen atmosphere are shown in Fig. 2. The peaks in the diffraction pattern from all these alloys can be consistently indexed based on the fcc δ-TiN phase (based on the NaCl structure), bcc β, and hcp α phases. Ti–V alloys sintered under a pure argon atmosphere exhibit only bcc β and hcp α phases, without any δ-TiN phase. The Ti–V–N$_{1300}$ alloy also show bcc β and hcp α phases, with no sign of δ-TiN. However in this alloy, lattice parameter measurement of the α phase shows that its c/a ratio is more than that expected for pure Ti. The higher c/a value is a clear indication of nitrogen enrichment in the hcp α phase. Moreover, the experimentally measured value of 1.61 is identical to the value reported for α-TiN$_{0.3}$ phase based on International Centre for Diffraction data (ICDD) files obtained from Joint Committee of Powder Diffraction Standards (JCPDS) [12,15,47]. Similar observations were found in case of a previous study on LENS™ deposited Ti–Mo–N alloy [15]. Thus, this phase is a nitrogen enriched α(Ti,N) hcp phase (space group P6$_3$/mmc) wherein the nitrogen atoms are expected to occupy octahedral interstitial sites within the hcp lattice. In contrast the Ti–V–N$_{1400}$ alloy clearly exhibits the presence of the fcc δ-TiN phase along with bcc β and hcp α titanium phases. The presence of the δ phase in this composite is probably due to the higher (i.e. 1400 °C) sintering temperature compared to Ti–V–N$_{1300}$ alloy that was sintered at 1300 °C, keeping other processing parameters nominally constant. Thus it appears that temperature is a governing factor in determining the formation of δ-TiN in these composites.

Fig. 3(a) and (b) shows the microstructure of the Ti–V–N$_{1300}$ alloy sintered at 1300 °C for 60 min under a pure nitrogen atmosphere in the SPS system. The microstructure clearly exhibits two precipitate phases with rather different morphologies. The coarser precipitates appear to exhibit an equiaxed/ globular morphology with curved interfaces separating them from the β matrix, suggesting that these interfaces are presumably incoherent or semicoherent in nature. Along with that finer scale α precipitates having an acicular or lath-like morphology are also present within the β-matrix. In comparison, while the lath-like α precipitates were present, the big equiaxed α precipitates were not present in case of the

Fig. 2. XRD pattern obtained from SPS sintered Ti–V–N alloys.

Ti–V$_{1300}$ sample prepared under a pure Ar atmosphere (Fig. 2c). Thus the introduction of N$_2$ during SPS processing results in the formation of a new equiaxed or globular α phase within the β matrix. XRD studies were conducted on this alloy and results show only two distinct phases, α(Ti,N) and β, present in the sample (Fig. 1). No substantial volume fraction of any third phase, specifically δ-TiN, was observed from the XRD patterns. Fig. 3(c) and (d) shows the microstructure of Ti–V–N$_{1400}$ alloy sintered at 1400 °C for 30 min under a pure nitrogen atmosphere in the SPS unit. From the backscattered contrast (atomic mass contrast) in the higher magnification SEM image in Fig. 3(d), three distinct phases with rather different morphologies can be clearly identified. The coarser dark precipitates appear to exhibit a more cuboidal morphology and are surrounded by a grey equiaxed phase with curved interfaces. The β matrix, exhibits a lighter contrast, and is interspersed with grain boundary α and α laths. XRD results from this composite showed three distinct phases: δ-TiN, α(Ti,N), and β (Fig. 2). Thus it can be deduced that the dark cuboidal precipitates observed in SEM micrographs correspond to the δ-TiN phase, which has the lowest atomic mass. These are surrounded by equiaxed precipitates of α(Ti,N) phase. This has been further validated via detailed TEM investigations carried out on the Ti–V–N$_{1400}$ sample and would be discussed later. The presence of the nitride phase at 1400 °C and not at 1300 °C may be due to higher diffusivity of nitrogen at higher temperatures leading to enough supersaturation in the single phase β to precipitate out δ-TiN. Subsequently during rapid cooling from 1400 °C to room temperature, globular α supersaturated with N$_2$ form around these δ-TiN precipitates. To validate this observation, Fig. 3(e) and (f) shows the microstructure of Ti–V–N alloy sintered at 1400 °C for a shorter time period (5 min) under a nitrogen atmosphere. The higher magnification image (Fig. 3(f)) clearly shows cuboidal δ-TiN precipitates surrounded by equiaxed α(Ti,N) precipitates. The only measurable difference is the size and volume fraction of δ-TiN precipitates which are much smaller than those observed after 30 min of sintering at 1400 °C. This finding proves that δ-TiN precipitates form primarily at 1400 °C and the holding time plays an important role in coarsening of these precipitates. Based on area fraction measurements using the Image J software, the approximate volume fraction of δ-TiN precipitates, in the Ti–V–N alloy sintered at 1400 °C for 30 min, is 25%. However the details of this transformation need to be investigated further.

3.3. Vickers microhardness results

The Vickers microhardness values for the Ti–V alloys that were sintered at 1100 °C, 1200 °C, 1300 °C and 1400 °C in pure Ar as well as N$_2$ atmospheres have been plotted in Fig. 4. The binary Ti–V alloys (lower blue curve), SPS sintered under a pure Ar atmosphere, exhibit an average hardness of ~450 HV. When the Ti–V alloys were spark plasma sintered at different temperatures in an inter argon atmosphere, the resulting microstructure consisted of only α and β phases and no nitrogen enriched or nitride phases were formed. Furthermore, there was no substantial change in either the prior β grain size or the size scale and distribution of α precipitates between Ti–V alloys sintered at different temperatures within the range of 1100–1400 °C. Therefore in the SPS processed Ti–V, the sintering temperature did not appear to have any significant effect on the microhardness. In contrast the Ti–V alloys that were sintered in pure N$_2$ atmosphere (Ti–V–N alloys) show an overall increase in hardness (upper red curve). For example, sintering at 1300 °C in a reactive nitrogen atmosphere exhibits the relatively higher microhardness value of ~680 HV, which is ~50% higher as compared with the Ti–V alloy sintered in a pure Ar atmosphere under similar conditions. Such an increase in hardness after sintering at 1100 °C, 1200 °C, and 1300 °C, can be attributed to the
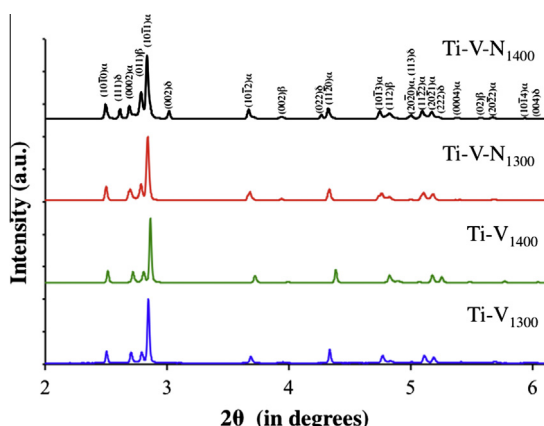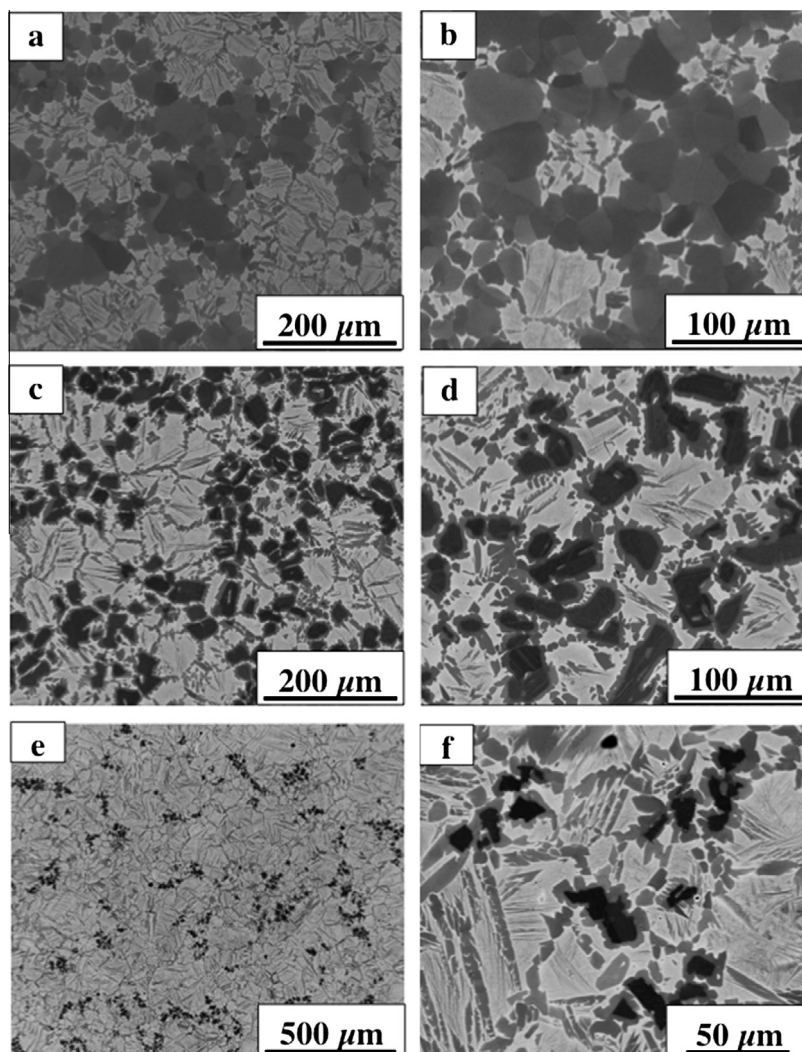
Fig. 3. (a) Low and (b) high magnification backscatter SEM image of SPS sintered Ti–V–N$_{1300}$ Alloy. (c) Low and (d) high magnification backscatter SEM image of SPS sintered Ti–V–N$_{1400}$ alloy (holding time: 30 min). (e) Low and (f) high magnification backscatter SEM image of SPS sintered Ti–V–N$_{1400}$ alloy (holding time: 5 min).
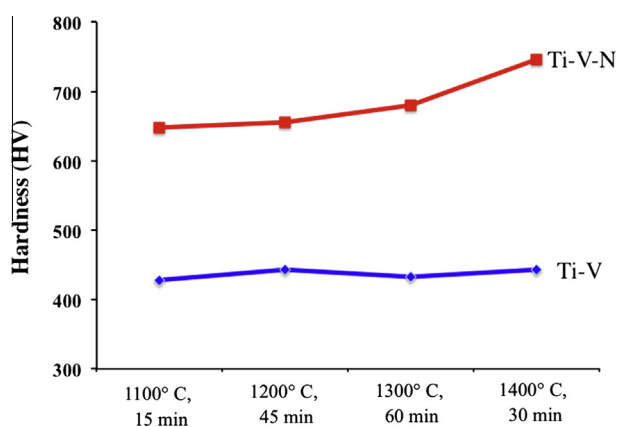

Fig. 4. A plot showing the variation in Vickers microhardness values for SPS sintered Ti–V and Ti–V–N alloys.

formation of the α-(Ti,N) phase, which is enriched in N$_2$. There is additional increase in hardness of the Ti–V–N alloy that is sintered at 1400 °C (~780) HV, which is ~25% higher than other Ti–V–N alloys. The increase can be attributed to the combined effect of δ-TiN phase as well as equiaxed α(Ti,N) precipitates.

3.4. Orientation imaging microscopy analysis

Fig. 5(a) shows a backscatter SEM image of the Ti–V–N$_{1300}$ specimen, sintered at 1300 °C for 60 min under pure nitrogen atmosphere, where the larger equiaxed α(Ti,N) phase along with lath-like α precipitates are clearly visible (marked by black circles). A detailed analysis of these two types of precipitates was carried out using orientation microscopy (OM) studies. The region that was used for setting up the EBSD scan has been marked by a red rectangle in Fig. 5(a). Fig. 5(b) shows [1] the pseudo-colored OIM™ map of this region wherein both α(Ti,N) and β phases have been attributed colors based on their respective Euler angles, as indicated by the stereographic triangles in Fig. 5(c). Also Fig. 5(d) shows the overall phase map of the same region, with the red-colored regions corresponding to the hcp α precipitates, and the green colored regions corresponding to the bcc β matrix phase. Comparing Fig. 5(a–d), it is interesting to note that the single α(Ti,N) grain (marked by bold black circle) is actually comprised of differently oriented smaller equiaxed regions. However the α -laths present on the right (marked by black dashed circle) appear to be of same

---

[1] For interpretation of color in Figs. 5 and 8, the reader is referred to the web version of this article.
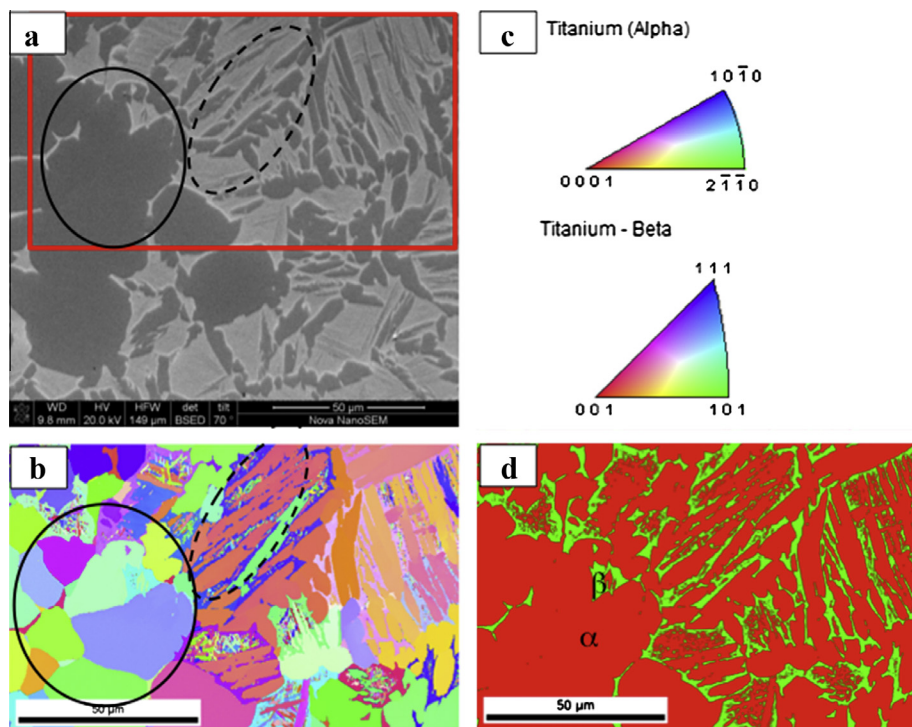
Fig. 5. (a) Backscatter SEM image and corresponding (b) pseudo-colored OIM™ map & (c) phase map of a region in Ti–V–N$_{1300}$ alloy where the EBSD scan was carried out. On both/all the images, equiaxed α cluster and also an inter-granular secondary α precipitate has been marked.

orientation. A more detailed analysis of equiaxed α(Ti,N) clusters and α laths have been shown in Figs. 6 and 7 respectively. The pseudo-colored OIM™ map of α(Ti,N) clusters obtained from Fig. 5(a) has been isolated and is shown in Fig. 6(a). The cluster shown in Fig. 6(a) comprises seven distinctly oriented α precipitates, marked 1 through 7 on the OIM™ map with individual colors based on their orientations, as per the stereographic triangle in Fig. 5(c), and their corresponding (0001) α poles have been marked in Fig. 6(b). The {11$\bar{2}$0} α poles for the same seven precipitates as well as {011}β and {111} β pole figures for the surrounding β grain are also shown in Fig. 6(b). It is interesting to note that none of the (0001) α poles lie close to any of the {011}β poles. This observation clearly indicates that the Burgers orientation relationship (OR) between α(Ti,N) and β does not exist in this case. Interestingly, the entire region lies within a single β grain. EBSD-OIM™ analysis of an inter-granular α precipitate exhibiting a more lath-like morphology is shown in Fig. 7. Along with the pseudo-colored map in of the precipitate in Fig. 7(a), the (0001) α and{11$\bar{2}$0} α pole figures as well as {011}β and {111} β pole figures for the surrounding β grain are also shown in Fig. 7(b). From the pole figures it is evident that the α precipitate and the surrounding β grain have a Burgers orientation relationship (0001) α //{011} β marked by green circles and ⟨11$\bar{2}$0⟩ α // ⟨111⟩ β depicted as red squares. Similar studies were conducted for other α laths and in all cases Burgers orientation relationship between these laths and surrounding β matrix was observed.

Orientation Microscopy (OM) studies were also conducted on Ti–V–N$_{1400}$ specimen, sintered at 1400 °C for 30 min under pure nitrogen atmosphere. As determined from SEM and XRD results, along with α(Ti,N) and β phases, δ-TiN was also present in the microstructure. These TiN precipitates not only restrict β grain growth but may also act as heterogeneous nucleation sites for α precipitation. Crystallographic orientation relationships between α, β, and δ phases were investigated in detail via EBSD-OIM™ studies. Interestingly, the morphology of α precipitates that form around these nitrides appear to be equiaxed. Typically, the initial nucleation of α during the solid state β → β + α on slow cooling

takes place at prior β grain boundaries. These grain boundaries act as heterogeneous nucleation sites for the formation of grain boundary α allotriomorphs. However, in case of the Ti–V–N composites, in addition to the prior β grain boundaries, the δ TiN precipitates are also likely to act as α nucleation sites. A backscatter SEM image of the Ti–V–N$_{1400}$ alloy showing all three phases is seen in Fig. 8(a). The exact region where EBSD analysis was carried out is shown using a red square in the same figure. Fig. 8(b) shows the corresponding pseudo-colored OIM™ map of this region wherein all δ-TiN, α(Ti,N), and β phases have been attributed colors based on their respective Euler angles, as shown by the stereographic triangle in Fig. 8(c). Also Fig. 8(d) shows the overall phase map of [1]the same region, with the yellow-colored regions corresponding to the fcc δ-nitride precipitates, the red-colored regions corresponding to the hcp α precipitates, and the green colored regions corresponding to the bcc β matrix. Similar to Fig. 5, in case of Fig. 8(a) and (b), one can clearly see that the α region surrounding a δ-nitride particle (shown by a yellow circle at the center of both Fig. 8(a) and (b)) consists of a cluster of several small precipitates of different orientations. However the broken α lath encircled by a yellow dotted ellipse, in the top left of the image in Fig. 8(b) consists of just one orientation. A more detailed analysis of the all these precipitates have been conducted and is shown in Figs. 9 and 10. The pseudo-colored OIM™ map of the region marked by a yellow circle in Fig. 8(b) has been shown in greater detail in the OIM man shown in Fig. 9(a), and corresponding δ, α, and β pole figures are shown in Fig. 9(b). The map clearly show a single orientation of δ-TiN precipitate and three distinct variants of α(Ti,N) precipitates surrounding the δ-TiN precipitate. These three α(Ti,N) precipitates are marked as 1 through 3 on the OIM™ map, and their corresponding (0001) α poles have been marked on the pole figure. In addition, the {11$\bar{2}$0} α, {111}δ, {110}δ, {011}β and {111}β pole figures are also shown in Fig. 9(b). It is interesting to note that all the three (0001) α poles (1, 2, 3) lie far from corresponding {011} β poles. Also, further analysis of the EBSD-OIM™ dataset revealed that the measured misorientation angles between any two adjacent
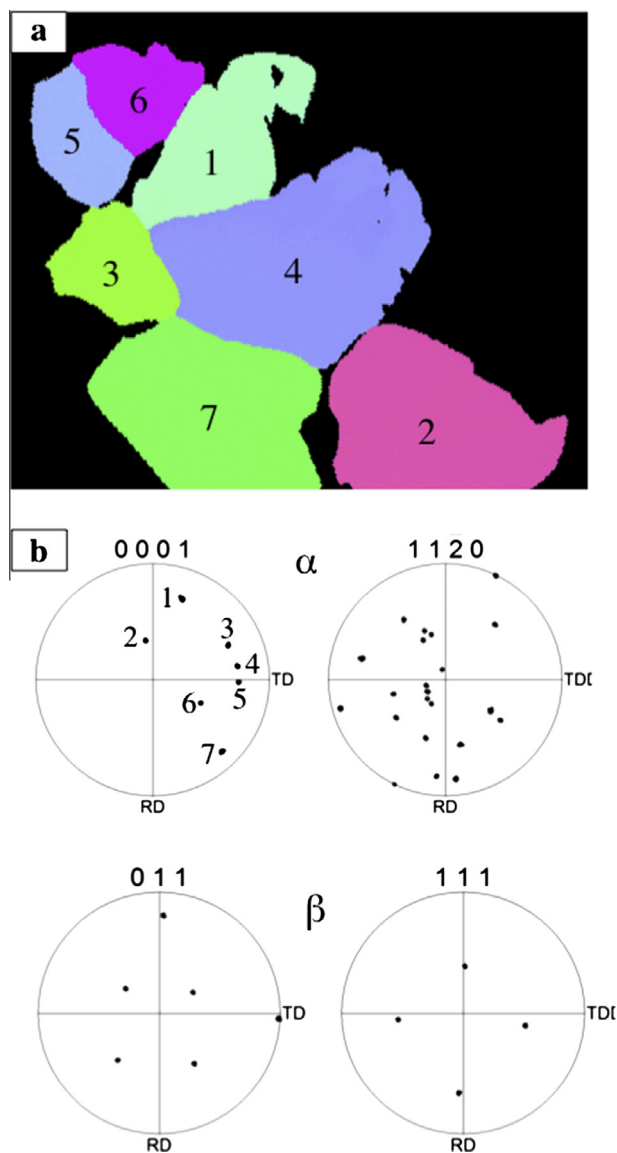
Fig. 6. (a) Pseudo-colored OIM™ map and (b) corresponding α and β pole figures of α cluster.

Fig. 7. (a) Pseudo-colored OIM™ map and (b) corresponding α and β pole figures of inter-granular α.

α precipitates shown in Fig. 9(a), corresponds to a rotation of ~70° about their common {11$\bar{2}$0} pole. Thus it is quite evident that Burgers OR between α and β is not observed in this case. Also there seems to be no OR between the δ nitride and β matrix as well, indicating that the nitride phase is unlikely to have nucleated from the β grains. However, from the pole figure plots it is clear that all three α precipitates do have a definite OR with the nitride particle, given by [(0001)α // (111) δ and ⟨11$\bar{2}$0⟩ //[110]δ]. The corresponding (0001)α // (111)δ poles are shown in Fig. 9(b), using green circles, red squares and blue triangles. Thus as suspected previously, the δ-TiN phase appears to be acting as the nucleation site for these α(Ti,N) precipitates. Since these α(Ti,N) precipitates do not exhibit the Burgers OR with the adjacent β grain as well as have a larger c/a ratio due to their high nitrogen content, they grow as equiaxed precipitates. This observation is similar to case of α(Ti,N) precipitates in the Ti–V–N$_{1300}$ alloy. Fig. 10(a) shows a magnified view of the α lath, marked by an ellipse in the top left corner of Fig. 8(b). The pole figure analyses shown in Fig. 10(b) clearly exhibits a Burgers OR between this α lath and the surrounding β matrix given by (0001) α // {011}β and ⟨11$\bar{2}$0⟩ α // ⟨111⟩ β. This α precipitate grows with a lath-like morphology, presumably with a
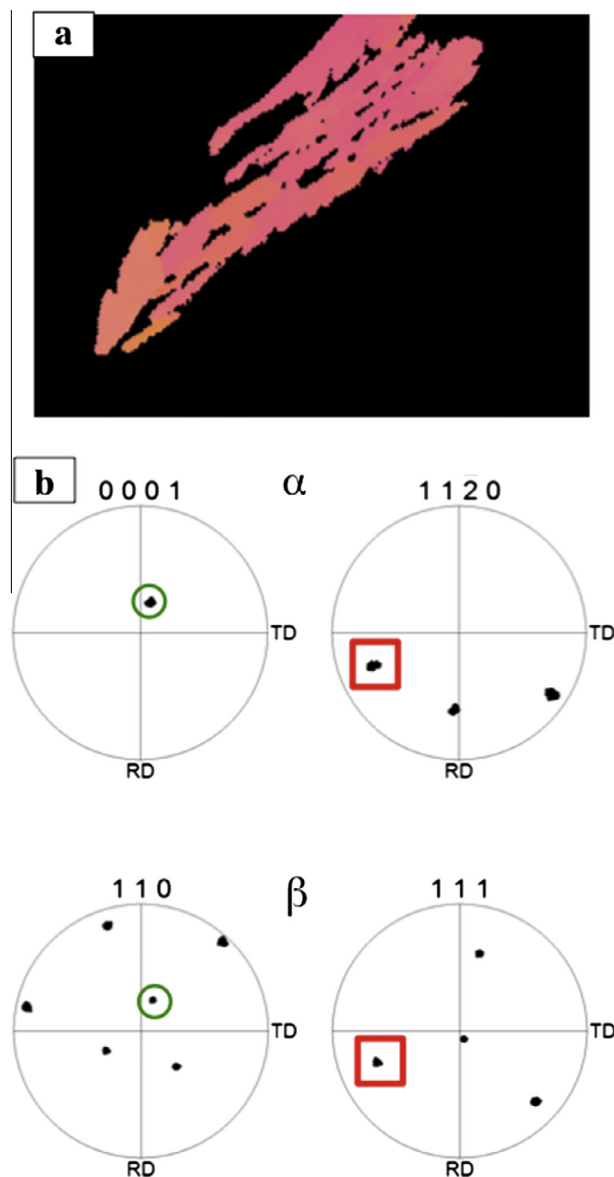
semi-coherent α/β interface along the broad face of the lath. These observations suggest that α nucleating and growing off the δ precipitates usually exhibits the equiaxed/globular morphology, unlike the widmanstattern α lath side plates growing from grain boundary α allotrimorphs or α nucleating homogeneously within the β matrix. The present study clearly elucidates the role of crystallographic orientation relationships between the δ, α, and β phases on the morphology of α precipitates in Ti–V–N$_{1400}$ alloys.

3.5. Transmission electron microscopy and orientation imaging microscopy analysis

Site-specific TEM samples were extracted from the Ti–V–N$_{1400}$ alloy with the help of a dual-beam focused ion beam instrument (FIB). A montage of several low magnification bright field scanning transmission electron microscopy (STEM) images, acquired using a high-angle annular dark-field (HAADF) detector, showing the entire FIB lift-out sample, is shown in Fig. 11(a). Three main areas were primarily analyzed and marked on the image: "region 1" corresponding to refined and faceted lath-like α precipitates within

7

Fig. 8. (a) Backscatter SEM image and corresponding (b) pseudo-colored OIM™ map & (c) phase map of a region in Ti–V–N$_{1400}$ alloy where the EBSD scan was carried out. On both/all the images, cuboidal δ nitride surrounded by equiaxed α within β matrix and also inter-granular secondary α precipitate has been marked.

the β matrix, "region 2" corresponding to equiaxed α precipitates that are nucleated from δ-TiN, and "region 3" corresponding to the δ-TiN precipitate. A bright field TEM image of region 1 (Fig. 11(b)) shows fine scale α precipitates dispersed within β matrix. The laths are ∼0.2 μm thick and 0.5–1 μm long. Fig. 11(c) shows a selected area diffraction pattern from primarily the β matrix with some overlapping α laths that were within the field of view of the selected area aperture. In addition to the primary (110), (002) and (112) reflections from the β matrix, there are additional reflections at $^1/_2$ (112), $^1/_3$ (112) and $^2/_3$ (112) positions. The streak at $^1/_2$ (112) is probably due to some fine scale α laths that are favorably oriented (Burgers OR) for diffraction. However, the additional reflections at $^1/_3${112} and $^2/_3${112} positions cannot be attributed to either the β matrix or the fine scale α precipitates; rather they are due to fine scale ω phase precipitation within the β matrix [48]. Therefore, in region 1 there is a co-existence of both fine scale α and ω precipitates within the β matrix. The dark field (DF) image from region 2 is shown in Fig. 11(d), and the corresponding SAD pattern from the same region is shown in Fig. 11(e). Both the images clearly show that this equiaxed phase in the Ti–V–N$_{1400}$ alloy is hcp α(Ti,N), oriented along [11$\bar{2}$0]α zone axis. From the location of (0002)α and (10$\bar{1}$0)α reflections, the lattice parameters of this phase was calculated and the c/a ratio was found out to be 1.61 (Table 2). This is consistent with the XRD results shown in Fig. 1.

Fig. 12(a) shows a higher magnification BF image of region 3 (referring to Fig. 11(a)), primarily consisting of a single δ-TiN precipitate. Interestingly, within this nitride precipitate, a cluster of fine scale lath-like precipitates of a second phase, oriented along different directions, is clearly visible. Selected area diffraction

patterns from within one of the lath-like precipitates (marked as 3a in Fig. 12(a)) and from within the nitride precipitate (marked as 3b in Fig. 12(b)) are shown in Fig. 12(b) and (c) respectively. While the SAD pattern in Fig. 12(b) can be consistently indexed as the [11$\bar{2}$0] zone axis of α, the pattern in Fig. 12(c) can be indexed as the [110] zone of the δ TiN phase. Comparing the two diffraction patterns clearly shows that the (1$\bar{1}$1)δ and (0002)α reflections are parallel to each other, leading to the OR between the δ-TiN and α laths: [110] δ//[11$\bar{2}$0] α and (1$\bar{1}$1)δ//(0002)α. This confirms firstly, that the fine scale lath-like precipitates within the δ-TiN grain belong to the α phase, and secondly, that these α laths lying within the δ TiN grain have nucleated from it during the cooling process. A DF image, recorded from one of the α reflections in the diffraction pattern, shown in Fig. 12(d) clearly reveals the lath-like morphology of the α phase, where one variant is in diffracting condition, while laths formed in at least two other directions can be identified (marked by white arrows in Fig. 12(d)).

3.6. Evolution of microstructure in SPS sintered Ti–V–N alloys

Spark plasma sintering (SPS) is a solid-state processing tool, where the sintering temperature is typically much lower than the material's melting temperature. In this study, based on the sintering temperature, that the Ti–V–N alloys are subjected to, one can predict the phase transformations that occur in these alloys.

At 1300 °C when Ti and V powders are sintered in the presence of nitrogen gas (Ti–V–N$_{1300}$ alloy), the observed microstructure consists of hcp α(Ti,N) and bcc β phases. EBSD results suggest that the equiaxed α(Ti,N) precipitates are composed of a cluster of differently oriented α variants which is formed in the same β grain.

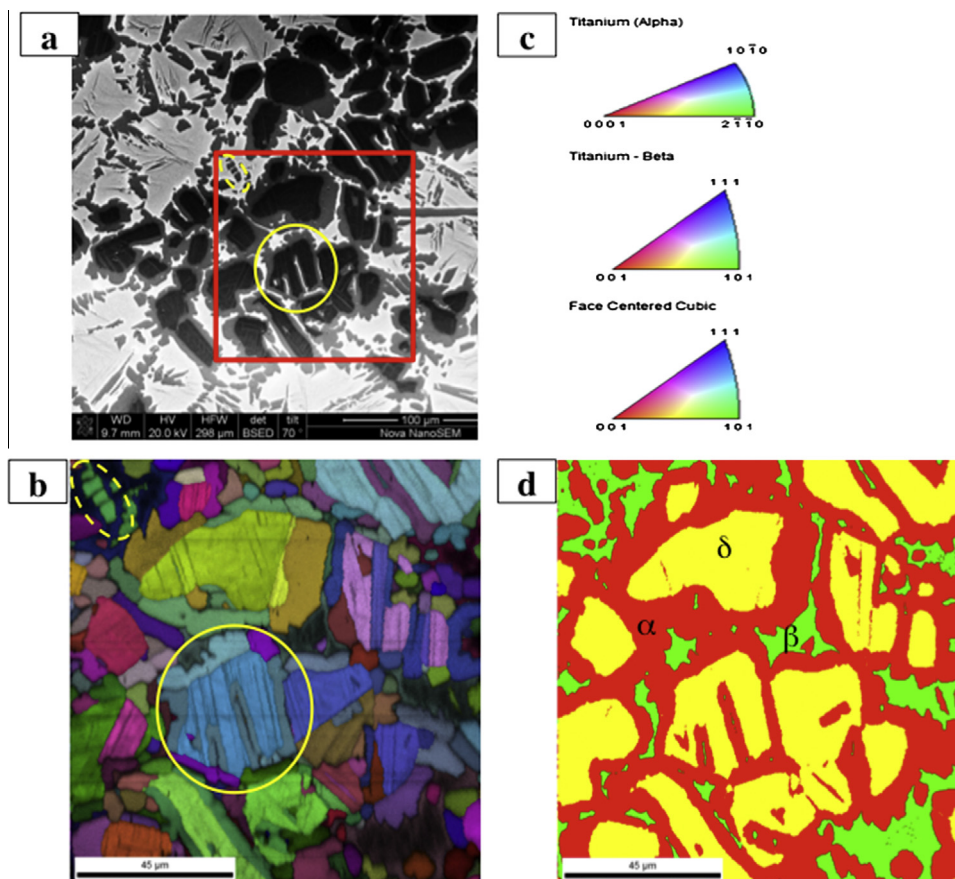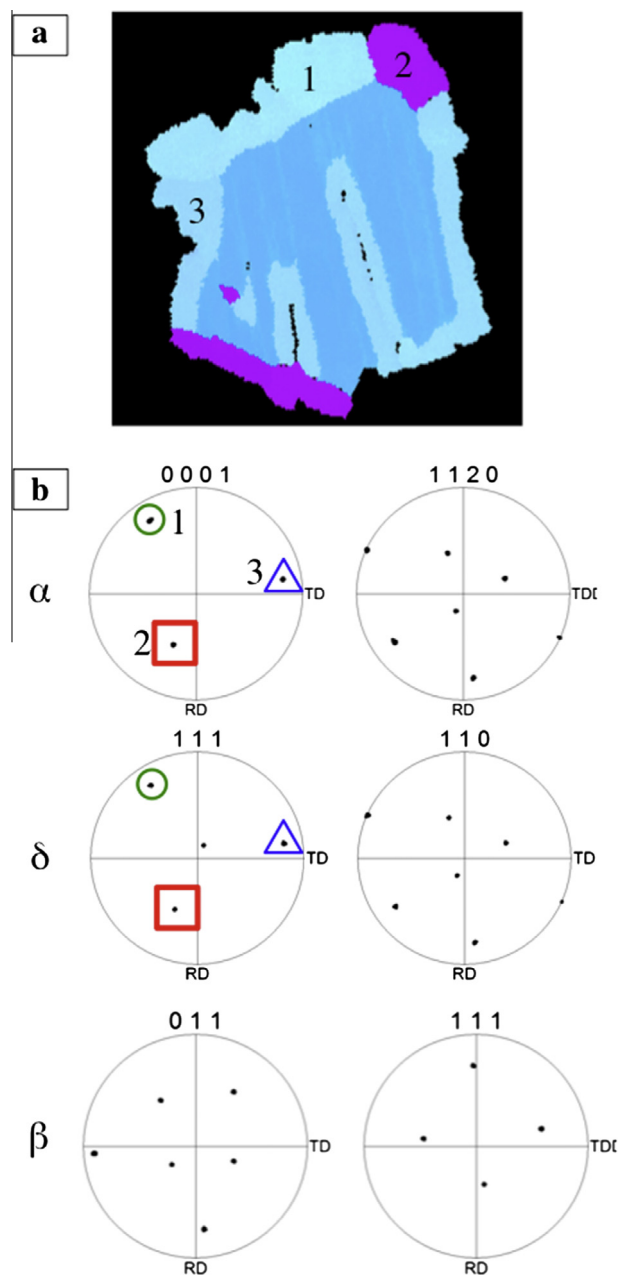**Fig. 9.** (a) Pseudo-colored OIM™ map and (b) corresponding δ, α, and β pole figures of cuboidal δ nitride surrounded by equiaxed α within β matrix.

Fig. 10. (a) Pseudo-colored OIM™ map and (b) corresponding α and β pole figures of inter-granular α.

However no Burgers OR is observed in this case between any of the α(Ti,N) precipitates and the surrounding β matrix. This and other similar regions consisting of a cluster of differently oriented α variants, possibly nucleated within the same β grain and may have had Burger OR at the early stages of their growth. However, one can predict that as these α precipitates grow and coarsen further, two things happen. Firstly the α clusters grow and imping onto each other forming α/α boundaries (with or without a thin βwetting layer). Secondly, as the precipitates grow in size, it is amenable for nitrogen to diffuse into the hcp interstitial sites, resulting in its higher c/a ratio (XRD results in Fig. 1 and Table 2). Thus nitrogen being a strong α stabilizer, naturally partitions strongly to the precipitating α phase, forming the α(Ti,N) phase. The V in contrast is a strong β stabilizer and hence partitions to the β matrix. As precipitates of α(Ti,N) grow within the β matrix during cooling, the strain energy increases rather rapidly due to the large misfit between the
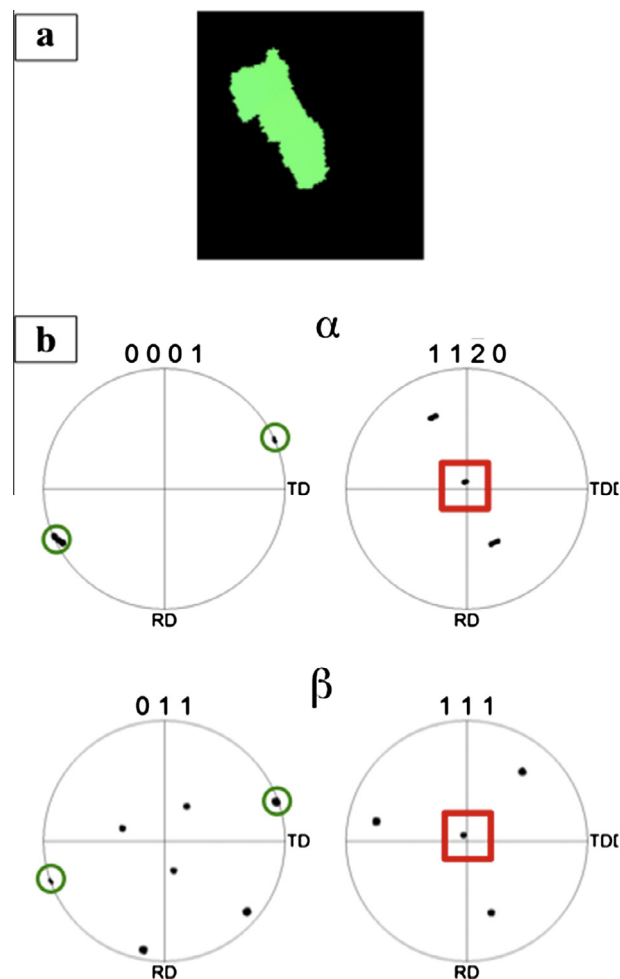
nitrogen rich α(Ti,N) phase and the V-rich surrounding β matrix. Changes in lattice parameters of the two phases, ultimately leads to the loss of coherency at the α(Ti,N)/β–Ti(V) interface, resulting in the formation of curved interfaces, as well as a more equiaxed morphology of these precipitates. Furthermore, there is a departure from the Burgers orientation relationship between the α(Ti,N) precipitates and the surrounding β matrix as these precipitates grow and coarsen. In contrast, the secondary α laths, which most probably nucleate at a later stage of cooling, exhibit Burgers OR with the matrix. Presumably, this secondary α contains a substantially lower amount of nitrogen as compared with the primary α(Ti,N) phase. Consequently, the secondary α precipitates exhibit a lower misfit with the β matrix, thus retaining an exact Burgers orientation relationship, as well as a more typical lath or plate-like morphology with faceted interfaces. One can chalk up the transformation sequence of Ti–V–N alloy at 1300 °C as follows:

β → β + *equiaxed* α(*Ti,N*) (at early stages of cooling from 1300 °C, does not show Burgers OR)
→β + *equiaxed* α(*Ti,N*) + *lath and grain boundary* α (at later stages of cooling from 1300 °C, does show Burgers OR).

The sequence of solid-state transformation in quite different when a mixture of titanium and vanadium powders are SPS treated at 1400 °C in an atmosphere enriched in nitrogen (Ti–V–N$_{1400}$ alloy). At this temperature, the β phase is supersaturated with nitrogen, leading to the formation of cuboidal δ-TiN precipitates

9

Fig. 11. (a) Scanning transmission electron microscopy (STEM) image of a site-specific sample made from Ti–V-$_{N1400}$ alloy, acquired using a high-angle annular dark-field (HAADF) detector. (b) Bright-field TEM image and (c) corresponding SAD pattern of fine scale α-lath within β matrix, also showing additional diffraction spots of ω phase corresponding to region 1. (d) Bright-field TEM image and (e) corresponding SAD pattern of an equiaxed α precipitates surrounded to cuboidal δ phase, corresponding to region 2.

Table 2
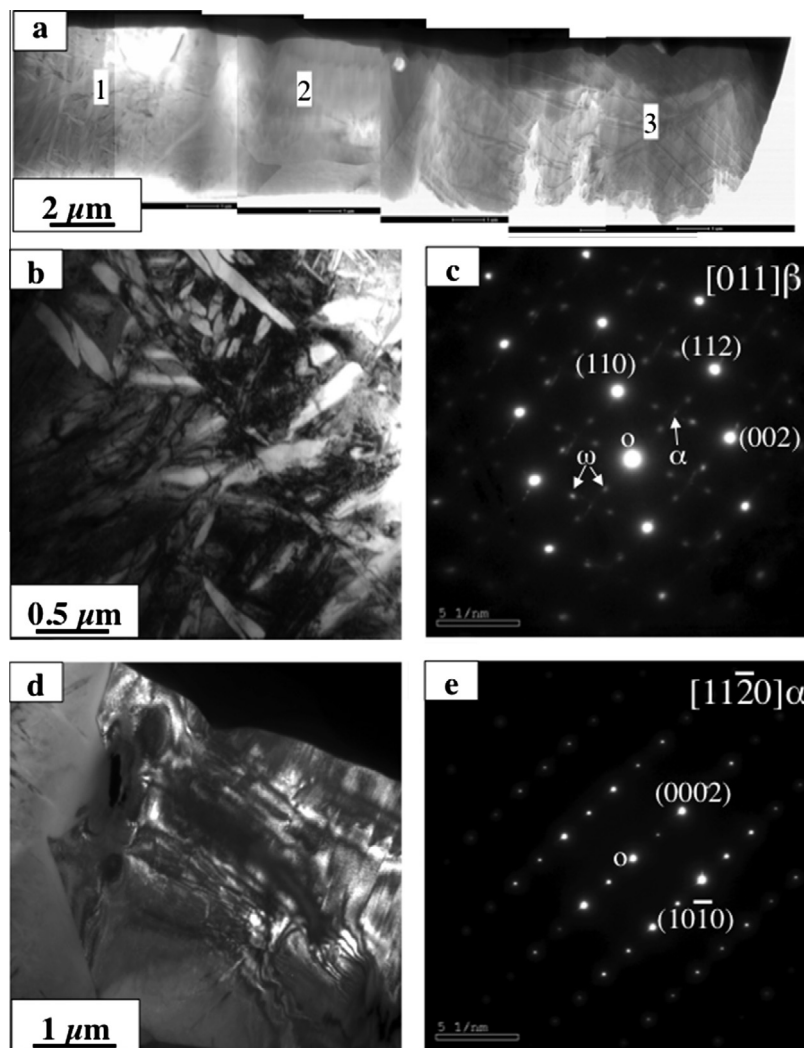Lattice parameters of alpha, beta, and delta phases in four different Ti–V alloys.

Alloy	$a\beta$ (Å)	$a\delta$ (Å)	$a\alpha$ (Å)	$c\alpha$ (Å)	c/a
Ti–V$_{1300}$	3.246	–	2.955	4.724	1.59
Ti–V–N$_{1300}$	3.250	–	2.959	4.754	1.61
Ti–V$_{1400}$	3.247	–	2.956	4.724	1.59
Ti–V–N$_{1400}$	3.250	4.243	2.964	4.775	1.61

along with the usual α(Ti,N) and β phases. The presence of an additional nitride phase at 1400 °C and not at 1300 °C is due to higher diffusivity of nitrogen at higher temperatures, leading to enough supersaturation in the single phase β to precipitate out δ-TiN. Comparison of short term (5 min) and long term (30 mins) SPS treatments do show that δ-TiN precipitates form primarily at 1400 °C and the holding time plays an important role in it's coarsening. Subsequently during the cooling of the β phase in the solid state, heterogeneous nucleation of the α phase from existing δ phase is initiated below the β transus temperature for this ternary Ti–V–N$_{1400}$ alloy. Also, EBSD as well as TEM studies show that these equiaxed α(Ti,N) precipitates tend to heterogeneously nucleate from δ precipitates that do not exhibit any specific OR with the

surrounding β matrix, and there is no OR between α precipitates and β matrix. While it cannot be confirmed based on the present experimental results, it is likely that there is some variant selection of the α(Ti,N) precipitates in their early stages of nucleation and growth, dictated by the orientation of the β matrix along with the δ-TiN precipitates. However when these α(Ti,N) precipitates become larger in size, due to the increase in nitrogen content, the lattice parameter of the α phase changes. This leads to a non-Burgers relationship between α and β phases. Again the change in α morphology from a typical lath-like to near equiaxed as well as presence of semi-coherent α/β interfaces can be attributed to the loss of Burgers OR. During cooling, the β matrix regions unaffected by the δ precipitates nucleate secondary lath-like α, exhibiting the Burgers OR with the β matrix. Thus the precipitation sequence at 1400 °C changes as follows:

β → β + δ-TiN (at1400 °C)
→β + δ-TiN + equiaxed α(Ti,N) (at early stages of cooling from 1400 °C, does not show Burgers OR)
→β + δ-TiN + equiaxed α (Ti,N) + lath and grain boundary α (at later stages of cooling from 1400 °C, does show Burgers OR).

10

Fig. 12. (a) High-magnification bright-field TEM images of lath-like α (region 3a) and cuboidal δ precipitates (region 3b) (b) SAD pattern obtained from lath-like α precipitates (region 3a) (c) SAD pattern obtained from δ precipitates (region 3b) (d) dark field TEM images of δ precipitates in which it nucleates the lath-like α shown by white arrows, corresponding to region 3.

Additionally, within the δ-TiN precipitates, fine nanometer scale lath-like α precipitates are formed, as clearly seen in Fig. 12(a) and (d). The formation of these internal α precipitates can be explained based on the differences in the minimum nitrogen content required to stabilize the δ-TiN phase at 1400 °C versus at room temperature. Thus, referring to the binary Ti–N phase diagram, shown in Fig. 13 [51], the minimum nitrogen content in a stable δ-TiN phase at 1400 °C is ~30 at%. In contrast, the minimum nitrogen content in a stable δ-TiN phase at 500 °C is ~40 at%. Therefore,

on cooling from 1400 °C to room temperature, the stable δ-TiN phase requires to increase its nitrogen content by over 10 at%. Consequently, the δ-TiN precipitates undergo an internal phase separation, wherein certain regions of these precipitates get enriched in nitrogen to stabilize the δ phase, whereas the adjacent regions are locally depleted in nitrogen. These local nitrogen depleted regions eventually form fine scale lath-like α precipitates within the same δ-TiN precipitate. Similar observations have been reported previously in case of δ-TiC precipitates in titanium base alloys such as Ti–6Al–4V [52].

4. Summary and conclusions

In situ nitridation of Ti–5 wt%V alloys has been achieved by the introduction of reactive nitrogen gas during the SPS sintering of these alloys from elemental powder blends. The SPS processing parameters have been optimized by changing the sintering temperature as well as hold time, based on V diffusion in bcc β-Ti, in order to obtain fully dense as well as reacted Ti–V alloys without any unreacted particles of Ti or V. Based on the optimization experiments, it was concluded that sintering at two temperatures, 1300 °C and 1400 °C, was found to be suitable for processing these nitrided composites. Ti–V–N$_{1300}$ and Ti–V–N$_{1400}$ alloys, sintered in N$_2$ atmosphere, exhibited much higher hardness and α volume fraction as compared with the Ti–V counterparts sintered in an Ar atmosphere. Specifically, the Ti–V–N$_{1300}$ alloy forms nitrogen-enriched equiaxed α(Ti,N) precipitates within the β matrix, along with fine scale secondary α precipitates. The higher c/a ratio of the α(Ti,N) precipitates, coupled with the V enrichment in the β matrix, results in a substantially large misfit, consequently leading to a loss of precipitate-matrix coherency during growth and

Fig. 13. Binary Ti–N phase diagram.

coarsening. This results in the α(Ti,N) precipitates adopting an equiaxed morphology, and they tend to aggregate into clusters. In contrast, the Ti–V–N$_{1400}$ alloy sintered at 1400 °C, showed stoichiometric δ-TiN precipitates that are surrounded by equiaxed α(Ti,N) precipitates. It was determined from this study that during the cooling process, the equiaxed α(Ti,N) precipitates tend to heterogeneously nucleate from the δ-TiN precipitates, maintaining a specific OR with the nitride precipitate, and not with the surrounding β matrix. TEM and EBSD experiments show that additional fine scale secondary α precipitates exhibiting a lath-like morphology (exhibiting a Burgers OR), and fine scale ω precipitates are also formed within the retained β matrix of this Ti–V–N$_{1400}$ alloy. The ability to introduce hard in situ δ-TiN as well as nitrogen enriched α(Ti,N) phase improves the microhardness properties of these alloys, which may help in improvement of their wear resistance.

Acknowledgements

References

[1] M.S. Selamat, T.N. Baker, L.M. Watson, Study of the surface layer formed by the laser processing of Ti–6Al–4V alloy in a dilute nitrogen environment, J. Mater. Process. Technol. 113 (2001) 509–515.

[2] M. Das, V.K. Balla, D. Basu, I. Manna, T.S. Sampath Kumar, A. Bandopadhyay, Laser processing of in situ synthesized TiB–TiN-reinforced Ti6Al4V alloy coatings, Scripta Mater. 66 (2012) 578–581.

[3] L. Cai, Y. Zhang, L. Shi, H. Yang, M. Xi, Research on development of in situ titanium matrix composites and in situ reaction thermodynamics of the reaction systems, J. Univ. Sci. Technol. B 13 (2006) 551–557.

[4] Z.D. Cui, S.L. Zhu, H.C. Man, X.J. Yang, Microstructure and wear performance of gradient Ti/TiN metal matrix composite coating synthesized using a gas nitriding technology, Surf. Coat. Technol. 190 (2005) 309–313.

[5] A.B. Kloosterman, J.T.M. De Hosson, Microstructural characterization of laser nitrided titanium, Scripta Mater. 33 (1995) 567–573.

[6] S. Mridha, T.N. Baker, Effects of nitrogen gas flow rates on the microstructure and properties of laser-nitrided IMI318 titanium alloy (Ti–4V–6Al), J. Mater. Process. Technol. 77 (1998) 115–121.

[7] T. Bell, W. Bermann, J. Lanagan, P.H. Morton, A.M. Staines, Surface engineering of titanium with nitrogen, Surf. Eng. 2 (1986) 133–143.

[8] D.M. Gordin, A. Guillou, I. Thibon, M. Bohn, D. Ansel, T. Gloriant, Duplex nitriding treatment of a beta-metastable Ti$_{94}$Mo$_6$ alloy for biomedical applications, J. Alloys Comp. 457 (2008) 384–388.

[9] L.M. Zou, C. Yang, Y. Long, Z.Y. Xiao, Y.Y. Li, Fabrication of biomedical Ti–35Nb–7Zr–5Ta alloys by mechanical alloying and spark plasma sintering, Powder Metall. 55 (2012) 65–70.

[10] S. Sathish, M. Geetha, N.D. Pandey, C. Richard, R. Asokamani, Studies on the corrosion and wear behavior of the laser nitrided biomedical titanium and its alloys, Mat. Sci. Eng. C 30 (2010) 376–382.

[11] V.K. Balla, A. Bhat, S. Bose, A. Bandopadhyay, Laser processed tiN reinforced Ti6Al4V composite coatings, J. Mech. Behav. Biomed. 6 (2012) 9–20.

[12] M. Geetha, U. Kamachi Mudali, N.D. Pandey, R. Asokamani, B. Raj, Microstructural and corrosion evolution of laser surface nitrided Ti–13Nb–13Zr alloy, Surf. Eng. 20 (2004) 68–74.

[13] A. Shenhar, I. Gotman, E.Y. Gutmanas, P. Dcheyne, Surface modification of titanium alloy orthopedic implants via novel powder immersion reaction assisted coating nitriding method, Mat. Sci. Eng. A 268 (1999) 40–46.

[14] C. Ponticaud, A. Guilou, P. Lefort, Direct gaseous nitridation of the ti–6Al–4V alloy by nitridation, Phys. Chem. Che. Phys. 2 (2000) 1709–1715.

[15] T. Borkar, S. Gopagoni, S. Nag, J.Y. Hwang, P.C. Collins, R. Banerjee, In situ nitridation of titanium–molybdenum alloys during laser deposition, J. Mater. Sci. 47 (2012) 7157–7166.

[16] A. Zhecheva, W. Sha, S. Malinov, A. Long, Enhancing the microstructure and properties of titanium alloys through nitriding and other surface engineering methods, Surf. Coat. Technol. 200 (2005) 2192–2207.

[17] D.M. Gordin, I. Thibon, A. Guilou, M. Cornen, T. Gloriant, Microstructure characterization of nitrided beta Ti–Mo alloys at 1400 °C, Mater. Charact. 61 (2010) 376–380.

[18] F. Torregrosa, L. Barrallier, L. Roux, Phase analysis, microhardness and tribological behavior of Ti–6Al–4V after ion implantation of nitrogen in connection with its application for hip-joint prosthesis, Thin Solid Films 266 (1995) 245–253.

[19] A.K. Shukla, R. Balasubramaniam, Effect of surface treatment on electrochemical behavior of CP Ti, Ti–6Al–4V and Ti–13Nb–13Zr alloys in simulated human body fluid, Corros. Sci. 48 (2006) 1696–1720.

[20] M. Geetha, A.K. Singh, R. Asokamani, A.K. Gogia, Ti based biomaterials, the ultimate choice for orthopedic implants-a review, Prog. Mater. Sci. 54 (2009) 397–425.

[21] F. Galliano, E. Galvanetto, S. Mischler, D. Landolt, Tribocorrosion behavior of plasma nitrided Ti–6Al–4V alloy in neutral NaCl solution, Surf. Coat. Technol. 145 (2001) 121–131.

[22] K.T. Rie, T. Stucky, R.A. Silva, E. Leitao, K. Bordji, J.Y. Jouzeau, D. Mainard, Plasma surface treatment and PACVD on Ti alloys for surgical implants, Surf. Coat. Technol. 74–75 (1995) 973–980.

[23] S.K. Wu, H.C. Lin, C.Y. Lee, Gas nitriding of an equiatomic TiNi shape memory alloy: II. Hardness, wear and shape memory ability, Surf. Coat. Technol. 113 (1999) 13–16.

[24] B.S. Yilbas, A.Z. Sahin, A.Z. Al-Garni, S.A.M. Said, Z. Ahmed, B.J. Abdulaleem, M. Sami, Plasma nitriding of Ti–6Al–4V alloy to improve some tribological properties, Surf. Coat. Technol. 80 (1996) 287–292.

[25] S. Piscanec, L.C. Ciacchi, E. Vesselli, G. Comelli, O. Sbaizero, S. Meriani, A.D. Vita, Bioactivity of TiN-coated titanium implants, Acta Mater. 52 (2004) 1237–1245.

[26] T.M. Muraleedharan, E.I. Metetis, Surface modification of pure titanium and Ti–6Al–4V by intensified plasma ion nitriding, Thin solid Films 221 (1992) 104–113.

[27] A.P. Serro, C. Completo, R. Colaco, F.D. Santos, C.L.D. Silva, J.M.S. Cabral, H. Araujo, E. Pires, B. Saramago, A comparative study of titanium nitrides, TiN, TiNbN and TiCN, as coatings for biomedical applications, Surf. Coat. Technol. 203 (2009) 3701–3707.

[28] I. Dion, F. Rouais, L. Trut, C. Baquey, J.R. Monties, P. Havlik, TiN coating: surface characterization and haemocompability, Biomaterials 14 (1993) 169–176.

[29] M.K. Harman, S.A. Banks, W.A. Hodge, Wear analysis of a retrieved hip implant with titanium nitride coating, J. Arthroplasty. 12 (1997) 938–945.

[30] L.A. Cyster, D.M. Grant, K.G. Parker, T.L. Parker, The effect of surface chemistry and structure of titanium nitride (TiN) films on primary hippocampal cells, Biomol. Eng. 19 (2002) 171–175.

[31] H. Pastor, Titanium–carbonitride-based hard alloys for cutting tools, Mat. Sci. Eng. A 105 (106) (1988) 401–409.

[32] C. Hu, L. Xin, L.M. Watson, T.N. Baker, Analysis of the phases developed by laser nitriding Ti–6Al–4V alloys, Acta Mater. 45 (1997) 4311–4322.

[33] A.I.P. Nwobu, R.D. Rawlings, D.R.F. West, Nitride formation in titanium based substrates during laser surface melting in nitrogen–argon atmosphere, Acta Mater. 47 (1999) 631–643.

[34] M.T. Raimondi, R. Pietrabissa, The in-vivo wear performance of prosthetic femoral heads with titanium nitride coating, Biomaterials 21 (2000) 907–913.

[35] H. Xin, C. Hu, T.N. Baker, Microstructural assessment of laser nitrided Ti–6Al–4V alloy, J. Mater. Sci. 35 (2000) 3373–3382.

[36] D.M. Gordin, T. Gloriant, G. Texier, I. Thibon, D. Ansel, J.L. Duval, M.D. Nagel, Development of a β-type Ti–12Mo–5Ta alloy for biomedical applications: cytocompatibity and metallurgical aspects, J. Mater. Sci. 15 (2004) 885–891.

[37] R. Orru, R. Licheri, A.M. Locci, A. Cincotti, G. Cao, Consolidation/synthesis of materials by electric current activated/assisted sintering, Mat. Sci. Eng. R 63 (2009) 127–187.

[38] Y. Song, Y. Li, Z. Zhou, Y. Lai, Y. Ye, A multi-field coupled FEM model for one-step-forming process of spark plasma sintering considering local densification of powder material, J. Mater. Sci. 46 (2011) 5645–5656.

[39] X. Song, X. Liu, J. Zhang, Neck formation and self-adjusting mechanism of neck growth of conducting powders in spark plasma sintering, J. Am. Ceram. Soc. 89 (2006) 494–500.

[40] W. Chen, U. Anselmi-Tamburini, J.E. Garay, J.R. Groza, Z.A. Munir, Fundamental investigations on the spark plasma sintering/synthesis process I. Effect of dc pulsing on reactivity, Mat. Sci. Eng. A 394 (2005) 132–138.

[41] U. Anselmi-Tamburini, S. Gennari, J.E. Garay, Z.A. Munir, Fundamental investigations on the spark plasma sintering/synthesis process II. Modeling of current and temperature distribution, Mater. Sci. Eng. A 394 (2005) 139–148.

[42] Z. Munir, D. Quach, Electric current activation of sintering: a review of the pulsed electric current sintering process, J. Am. Ceram. Soc. 94 (2011) 1–19.

[43] M. Omori, Sintering, consolidation, reaction and crystal growth by the spark plasma system (SPS), Mater. Sci. Eng. A 287 (2000) 183–188.

[44] Z. Munir, U. Anselmi-Tamburini, M. Ohyanagi, The effect of electric field and pressure on the synthesis and consolidation of materials: a review of the spark plasma sintering method, J. Mater. Sci. 41 (2006) 763–777.

[45] D.M. Hulbert, A. Anders, J. Andersson, E.J. Lavernia, A. Mukherjee, A discussion on the absence of plasma in spark plasma sintering, Scripta Mater. 60 (2009) 835–838.

[46] W. Yucheng, F. Zhengyi, Study of temperature field in spark plasma sintering, Mat. Sci. Eng. B 90 (2002) 34–37.

[47] J.P. Bars, D. David, E. Etchessahar, J. Debuigne, Titanium α-nitrogen solid solution formed by high temperature nitriding: diffusion of nitrogen, hardness, and crystallographic parameters, J. Metall. Trans. A 14A (1983) 1537–1543.

[48] R. Banerjee, P.C. Collins, D. Bhattacharyya, S. Banerjee, H.L. Fraser, Microstructure evolution in laser deposited compositionally graded α/β titanium–vanadium alloys, Acta Mater. 51 (2003) 3277–3292.

[49] W.F. Gale, T.C. Totmeier, Smithells Metals Reference Book, eight ed., Elsevier, Massachusetts, 2004.

[50] S.K. Sun, G.J. Zhang, W.W. Wu, J.X. Liu, T. Suzuki, Y. Sakka, Reactive spark plasma sintering of ZrC and HfC ceramics with fine microstructures, Scripta Mater. 69 (2013) 139–142.

[51] H. Baker, ASM Metals Handbook – Alloy Phase diagrams, vol. 3, ASM International, USA, 1992.

[52] D. Hu, T.P. Johnson, M.H. Loretto, Titanium precipitation in substoichiometric TiC particles, Scripta Mater. 30 (1994) 1015–1020.